Journal of Materials Chemistry A

Accepted Manuscript

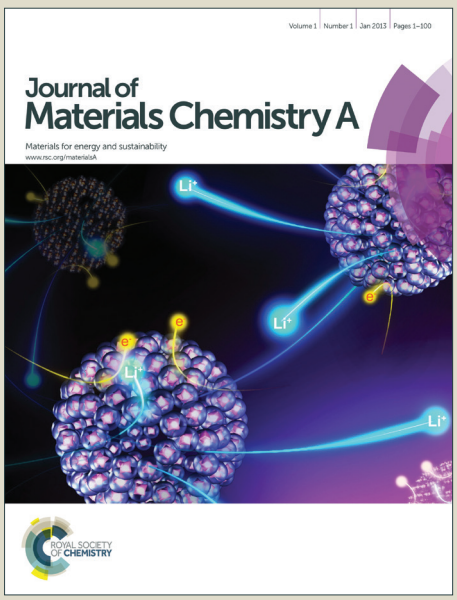

ROYAL SOCIETY OF CHEMISTRY

www.rsc.org/materialsA

Journal of Materials Chemistry A

RSCPublishing

ARTICLE

Integration of network-like porous $NiMoO_4$ nanoarchitectures assembled with ultrathin mesoporous nanosheets on three-dimensional graphene foam for highly reversible lithium storage

Cite this: DOI: 10.1039/x0xx00000x

Received 00th April 2015,
Accepted 00th April 2015

DOI: 10.1039/x0xx00000x

www.rsc.org/

Bo Wang, Songmei Li,* Xiaoyu Wu, Wenming Tian, Jianhua Liu, and Mei Yu

The interconnected ultrathin mesoporous nickel molybdate ($NiMoO_4$) nanosheets with a network-like porous structure supported on three-dimensional (3D) macroporous graphene network were successfully synthesized by a facile chemical vapor deposition (CVD) and subsequent hydrothermal route. The building block $NiMoO_4$ nanosheets are curved with a thickness as small as 3-5 nm, and randomly connected with the adjacent nanosheets to self-assemble into continuous, interconnected and porous architectures. The $NiMoO_4$ nanosheets supported on 3D graphene network could be directly evaluated as binder-free, integrated anodes for lithium-ion batteries (LIBs). Such unique 3D integrated architectures exhibited remarkable electrochemical performance with a high reversible capacity of 1155.54 mAh g^{-1} at a current densities of 200 mA g^{-1}, and an excellent cycling ability (89% of the initial reversible capacity remained after 120 cycles). The superior electrochemical performances could be attributed to the open network structure constituted of interconnected ultrathin mesoporous $NiMoO_4$ nanosheets directly grown on current collectors that could improve electron transport and enhance electrolyte diffusion efficiency.

1. Introduction

High-performance energy conversion and storage devices have attracted tremendous attention because of the rapid development of modern society and global economy, as well as the rapidly increasing global energy consumption coupled with the critical issue of climate change.[1,2] Among the intermediate energy storage devices, rechargeable lithium-ion batteries (LIBs) have become the dominant power source due to their high energy density, long cycle life, design flexibility and environmental benignity.[3-6] With the ever-growing demands for electric vehicles (EVs), hybrid electric vehicles (HEVs), and their wide range of applications (e.g., portable electronics, storage of renewable energies, smart grids, etc.), considerable efforts have been focused on designing and developing alternative electrode materials for next-generation LIBs with high-performance to power our future society.[7-10]

Transition metal molybdates, especially $NiMoO_4$, have gradually been considered as promising effective and scalable alternatives to the commercial graphite anode for LIBs in view of their excellent electrochemical performance, low-cost, environment benignity and abundance.[11-13] Most importantly, $NiMoO_4$ has been reported to demonstrate better performance than single-component metal oxides due to its multiple feasible oxidation states, large cell parameters and comparative higher electrical conductivity (10^{-6} S cm^{-1}).[14,15] Regrettably, despite of their distinguish advantages, they still suffer from their insufficient conductivity and the repetitively volume expansion/contraction during lithiation and delithiation processes, which can lead to rapid capacity fading and compromised high rate capability.[16,17] Therefore, rational design and facile synthesis of $NiMoO_4$-based electrode materials with novel architectures of high effective surface area and open path towards the electrolyte for highly reversible and high-rate lithium storage still remain a significant challenge.

Recently, an emerging attractive concept is to fabricate integrated, binder-free and light-weight LIB electrodes by directly coating, growing and depositing active materials on

Key Laboratory of Aerospace Advanced Materials and Performance of Ministry of Education, School of Materials Science and Engineering, Beihang University, Beijing, 100191, China.

E-mail: songmei_li@buaa.edu.cn; Fax: +86-10-82317103; Tel: +86-10-82317103

Electronic supplementary information (ESI) available. See DOI:

self-supported 3D porous conducting substrates without any binders or conductive agents. Among the various conducting substrates, three-dimensional graphene foam (3DGF) with continuously interconnected macroporous structures have been considered as promising current collectors because of their unique 3D network structure, high surface area, good flexibility and fast mass and electron transport kinetics.[18-20] And their 3D porous structure is ideal to serve as frameworks or scaffolds for the fabrication of monolithic composite and hybrid electrodes.[21,22] Inspired by this method, considerable efforts have been devoted to grow electroactive materials directly on 3DGF as binder-free electrodes for advanced LIBs.[23-25] Compared with the traditional casting electrodes of powder materials, the as-obtained active material@3DGF hybrid electrodes with desired architectures and properties take the key advance to realize their extensive potential applications for flexible electronics and energy-related devices.[26,27] Based on the above considerations, it is of great significance to develop facile and simple methods to achieve a robust 3D graphene-backboned $NiMoO_4$ architectures with superior electrochemical performances.

Herein, a novel interconnected network-like $NiMoO_4$ nanoarchitecture assembled with ultrathin and mesoporous nanosheets are successfully coupled on 3D graphene foam with robust adhesion, which is directly used as a binder-free electrode for electrochemical evaluation. The obtained network-like $NiMoO_4$ coupled on 3DGF is denoted as $NiMoO_4$@3DGF, in which ultrathin $NiMoO_4$ nanosheets with thickness of 3-5 nm build network-like blocks of 3D architectures. Benefiting from the interconnected conducting networks of 3DGF and $NiMoO_4$ sheets confined firmly on graphene foam to form network-like structure, the $NiMoO_4$@3DGF electrode exhibits high specific capacity and excellent cycling stability even under high current densities compared to binder-containing counterparts.

Experimental

Materials and Methods

Growth of the 3DGF: For a typical run, Nickel foams (NF, Lyrun Co., Ltd.) with areal density of ~0.038g cm^{-1} and porosity of ~97.3%, were used as 3D scaffold templates for the CVD growth of graphene. Prior to deposition, nickel foam cut into piece with the size of 2 cm×4 cm was degreased with acetone, etched with 1M HCl solution for 10 min, and then washed by deionized water and ethanol for 10 min with sonication, respectively. Then, the treated NF placed in a quartz tube, and heated from room temperature to 1050 ℃ in 50 min in a horizontal tube furnace (OTF-1200X) under Ar (50 sccm.) and H_2 (20 sccm.) gas flows. NF was maintained under 1050 ℃ for 30 min to clean their surfaces and to eliminate a thin surface oxide layer. Then CH_4 (5 sccm.) gas flow was introduced into the reaction tube to deposite graphene sheets on NF. After 120 min flow of reaction gas mixture, the samples were rapidly cooled to room temperature under Ar (50 sccm.) and H_2 (20 sccm.). After the growth, the graphene@Ni foam structure was etched in 2M $Fe(NO_3)_3$ solution in 80 ℃ for 12 hours to dissolve the nickel framework. Finally, 3DGF was obtained after washed with DI water and alcohol.

Synthesis and self-assembly of network-like $NiMoO_4$ nanoarchitectures@3DGF: The $NiMoO_4$@GF composites were prepared by a facile hydrothermal approach. In a typical experiment, 3 mmol of $Ni(CH_3COO)_2 \cdot 4H_2O$ and 0.6 g of $(NH_4)_6Mo_7O_{24} \cdot 4H_2O$ were dissolved into 90 mL of deionized water under constant magnetic stirring. Then 0.72 g of urea was added into the above solution. The mixture was kept at an intense ultrasonic treatment for a few minutes in order to form a light green solution and then transferred into polytetrafluoroethylene (PTFE) Teflon-lined stainless steel autoclave. The as-prepared 3DGF was immersed into the reaction solution and maintained at 150℃ for 6 h. After it was cooled down to room temperature, the graphene foam coated with a brown product was taken out from the autoclave, and washed by ultrasonication in deionized water and ethanol for a few minutes in order to remove the residual nanoparticle debris then dried in a vacuum oven at 60℃ for 12 h. Finally, the graphene foam with the as-grown hydrate precursors was annealed at 300℃ for 2 h in purity argon with the heating rate of 2℃/min to obtain the $NiMoO_4$@3DGF. For the comparison, $NiMoO_4$ spheres assembled from nanosheets were prepared by the same process only without adding the substrate of graphene foam.

Microscopic Characterization

The crystallographic structure of the as-prepared products were determined by a powder X-ray diffraction system (XRD, Rigaku D/max 2200PC) equipped with Cu Kα radiation (λ=0.15418 nm). The morphologies, chemical compositions, and the microstructures of the products were characterized by field-emission scanning electron microscope (FE-SEM, JEOL JSM-7500F) equipped with an energy dispersive X-ray spectrometry (EDS), transmission electron microscope (TEM, JEOL JEM-2100F), and X-ray photoelectron spectroscope (XPS, AXIS UTLTRADLD equipped with a dual Mg Ka-Al Ka anode for photoexcitation). The N_2 adsorption-desorption were determined by Brunauer-Emmett-Teller (BET) measurements using an ASAP-2010 surface area analyzer.

Electrochemical Performance Measurements

The electrochemical performance of the as-prepared products was performed using CR2025 coin-type cells. CR2025-type coin cells were assembled in an argon-filled glove box, in which oxygen and water contents were less than 1 ppm. In order to reduce the mass uncertainty of the electrodes, the as-prepared 3DGF and $NiMoO_4$@3DGF composites were punched in the form of 12 mm diameter disks, and then used directly as the working electrode without any conductive additive and polymer binder. Then, we took 10 pieces of samples (3DGF and $NiMoO_4$@3DGF composites, respectively) and weighed them together. The specific mass loading of the active material ($NiMoO_4$) for the testing electrodes was about 1～1.1 mg cm^{-2} calculated by the weight of the total mass. A metallic lithium foil served as both the counter electrode and the reference

electrode, a polypropylene (PP) microporous film (Celgard 2400) was used as the separator, and a solution of 1 M $LiPF_6$ dissolved in ethylene carbonate/dimethyl carbonate (EC:DMC=1:1 v/v) was used as electrolyte. In a control experiment, after the $NiMoO_4$ nanosheets spheres (NSS) powder was mixed with the conductive carbon black and polyvinylidene fluoride (PVDF) binder in a weight ratio of approximately 8:1:1, the slurry was directly coated on a copper foil and dried overnight in a vacuum oven at 60 ℃ to fabricate the electrode of $NiMoO_4$ NSS.

The galvanostatic charge-discharge and cyclic voltammetry (CV) measurements were conducted using a LAND CT2001A battery-testing instrument and a multichannel Arbin Instruments BT2000 (USA) unit in the voltage range of 0.005-3.0 V at room temperature (25±1℃). Electrochemical impedance spectroscopy (EIS) measurements were carried out in the frequency range from 100 kHz to 0.01 Hz on a PARSTRAT 2273 electrochemical measurement system under AC stimulus with a potential amplitude of 5 mV.

Results and discussion

A schematic illustration of the fabrication processes of $NiMoO_4$@3DGF composites is depicted in Scheme 1. The construction of hybrid $NiMoO_4$@3DGF nanostructure as a binder-free electrode mainly involves two key steps. In the first step, a porous structure with an interconnected 3D scaffold of Ni foam was served as a template for the chemical vapor deposition of graphene, followed by etching away the Ni skeleton to leave the free-standing 3DGF. The graphene foam consists of an interconnected flexible network of graphene as the fast transport channel of charge carriers for high electrical conductivity. In the second step, a brown thin layer of $NiMoO_4$ precursors ($NiMoO_4 \cdot xH_2O$) was firstly anchored and grown in situ onto the surface of the 3DGF under hydrothermal conditions. The network-like $NiMoO_4 \cdot xH_2O$ nanoarchitectures are anchored into the skeleton of 3DGF by spontaneous self-assembly of $NiMoO_4$ nanosheets. Finally, after the hydrothermal process, the $NiMoO_4$ precursors is thermally decomposed to light purple $NiMoO_4$ nanosheets supported on the 3DGF, which can be described by the simple dehydration reaction.

The phase structure of the as-prepared products was analyzed by X-ray diffraction. Fig. 1a shows the XRD patterns of the bare 3DGF, $NiMoO_4$@3DGF composites and the standard XRD pattern of monoclinic $NiMoO_4$. The XRD patterns of as-grown 3DGF display two typical diffraction peaks at 26.5 ° and 54.6 °, which is attributed to the (002) and (004) reflections of graphitic carbon, respectively (JCPDS card no. 75-1621). The absence of Ni diffraction peaks indicated the complete dissolution of the Ni foam. The highly crystalline structure of GF is favourable for the electron transfer and ion diffusion. In addition to the characteristic peaks from graphene, the presented new diffraction peaks in the XRD patterns of $NiMoO_4$@3DGF composites can be well indexed to the monoclinic structured $NiMoO_4$ with a space group of C2/m (JCPDS Card no. 45-0142).[28,29] In order to preclude the strong impact of graphene foam substrate on the XRD peak signals, the collected $NiMoO_4$ powers in the same reaction system were also checked by XRD. As indicated in Fig. S1 (Supporting Information), the XRD pattern confirms that all the diffraction peaks are well matched with the standard pattern of monoclinic $NiMoO_4$ (JCPDS Card no. 45-0142).[30]

Full nitrogen adsorption and desorption isotherms of the $NiMoO_4$@3DGF composites were measured to obtain the information on the pore size distribution and specific surface area. As shown in Fig. 1b, a type-IV isotherm with a distinct type-H3 hysteresis loop in the relative pressure range of 0.45-1.0 P/P_0 can be observed, which is ascribed to the presence of mesoporous structure in the sample. Accordingly, the specific surface area is calculated to be 56.44 $m^2 g^{-1}$ via the Brunauer-Emmett-Teller (BET) method. The mesoporous feature is further confirmed by the pore size distribution analysis. The sharp peak at a pore size range of 2-5 nm is attributed to mesoporous channels in $NiMoO_4$@3DGF architectures. Besides, the sharp peak at ~85 nm corresponds to macropores. Such a high specific surface area of $NiMoO_4$@3DGF composites with massive mesopores and macropores can provide the possibility of efficient transport of electrons and ions, and can also buffer the volume change during

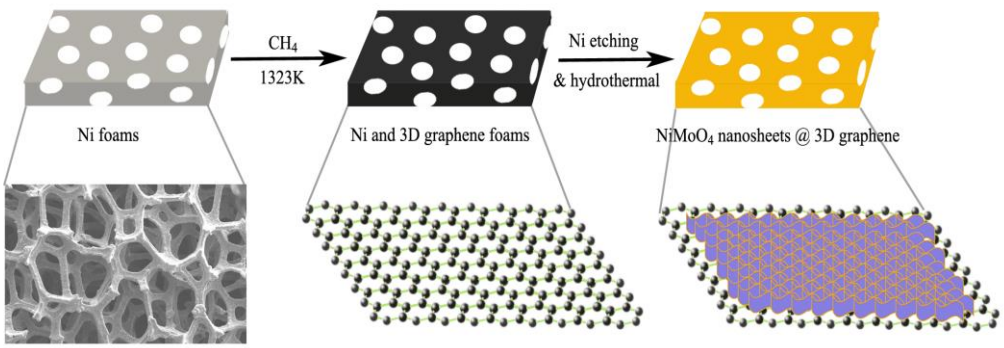

Scheme 1. Schematic illustration of the synthesis of $NiMoO_4$@3DGF composites.

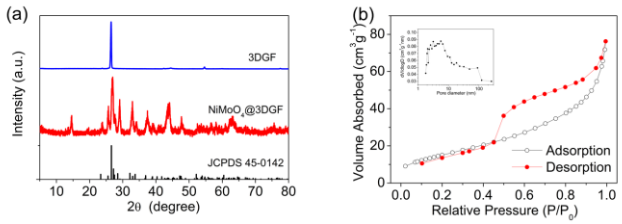

Fig. 1 (a) XRD patterns of the as-prepared 3DGF, and $NiMoO_4$@3DGF composites, and the standard XRD pattern of monoclinic $NiMoO_4$. (b) N_2 adsorption/desorption isotherms, and the insert corresponding pore size distribution of $NiMoO_4$@3DGF composites.

charge/discharge process to protect the active materials, leading to high electrochemical capacity of the electrode material.

The morphology and microstructure of the as-prepared products were evaluated by scanning electron microscopy (SEM). After the removal of the Ni template, graphene replicated the 3D network and the porous structure of the pristine Ni foam, without collapsing and cracking (As shown in Fig. 2a). The 3DGF with smooth surface before $NiMoO_4$ growth, and the width of the graphene skeleton was about 150 to 200 μm (Fig. S2, Supporting Information). Fig. 2b-d show the typical SEM images of $NiMoO_4$@3DGF composites at different magnifications. After $NiMoO_4$ growth, the surface of the $NiMoO_4$@3DGF composites becomes rough compared to the smooth surface of the pristine 3DGF, as shown in Fig. 2b. From the magnified SEM images (Fig. 2c and d), it can be clear seen that the $NiMoO_4$@3DGF composites exhibit a highly interconnected and porous architectures, which is formed by numerous interconnected ultrathin $NiMoO_4$ nanosheets are uniformly and completely grown upon the whole 3D graphene skeleton. As shown in Fig. 2d, the building block nanosheets are curved with a large lateral sizes of ~ 200 nm, and randomly connected with the adjacent nanosheets to self-assemble into continuous and interconnected porous architectures, forming a large number of voids and electroactive sites. Such unique microstructure not only provided stable structure for the electrodes but also the high specific surface are for the ionic transportation and oxidation-redox reactions, as reported previously in the literatures.[31-33] The morphologies of bending, curling, and crumpling are due to the much larger lateral size than the thickness. The height of the $NiMoO_4$ nanosheets films supported on graphene skeleton is about 300 nm, as can be seen from the cross-section SEM image (Fig. 2e). The composition of the as-prepared products was confirmed by EDS analysis under a N_2 atmosphere. It is clear that there is no Ni element in the samples, which indicates that nickel has been completely dissolved (Fig. S3 Supporting Information). As shown in Fig. 2f, the C, Ni, Mo, and O peaks are observed in the EDS spectrum of the as-prepared $NiMoO_4$@3DGF composites, suggesting that the sample is mainly composed of C, Ni, Mo, and O. In strong contrast, in the absence of GF, the exact same synthesis process produced $NiMoO_4$ NSS of about 2.5-3 μm in diameter (Fig. S4 Supporting Information). Fig.

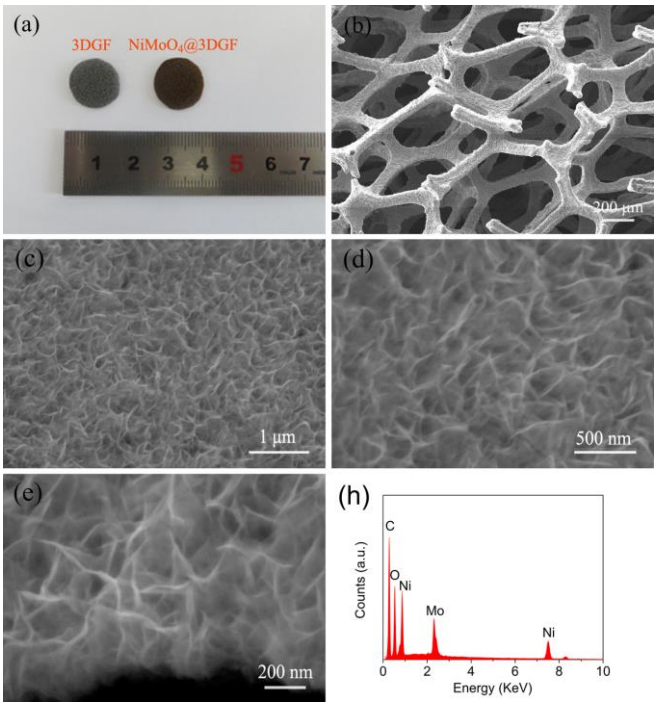

Fig. 2 (a) Photograph of as-prepared 3DGF and $NiMoO_4$@3DGF composites**.** (b-d) Typical SEM images of $NiMoO_4$@3DGF composites at different magnifications. (e) The EDS spectrum of the $NiMoO_4$@3DGF composites. (f) The cross-sectional SEM image of the $NiMoO_4$@3DGF composites. and (h) EDS spectrum of the as-synthesized $NiMoO_4$@3DGF composites.

S4a reveals $NiMoO_4$ NSS are constructed by interconnected thin nanosheets. The thickness of the hierarchical wall is about 10-15 nm, which is several five folds thicker than the nanosheets of $NiMoO_4$@3DGF composites (Fig. S4b Supporting Information). The obvious morphological difference highlights the important role of GF substrate as a novel support material in mediating the growth of nanomaterials.

The microstructure of $NiMoO_4$@3DGF composites was further evaluated by transmission electron microscopy (TEM). The low magnification TEM image (Fig. 3a) also confirm the interconnected network-like nanostructures of the products built up of flexible and ultrathin nanosheets, which is in good agreement with the SEM results. No material loss was observed after ultrasonication of the sample in solution for several minutes, indicating a robust mechanical adhesion of $NiMoO_4$@3DGF electrode, which is very promising for improving the electrochemical performance. In addition, the higher magnification TEM images shown in Fig. 3b clearly reveal the intrinsic wrinkles or corrugations of the cell sheets. Interestingly, ultrathin $NiMoO_4$ nanosheets with a thickness as small as 3-5 nm exhibit graphene-like morphology with transparent feature, Besides, a large number of mesopores (about 2-5 nm) are uniformly distributed on the nanosheets, further suggesting the ultrathin and mesoporous nature of the nanosheets (as shown in Fig. S5). The formation of the

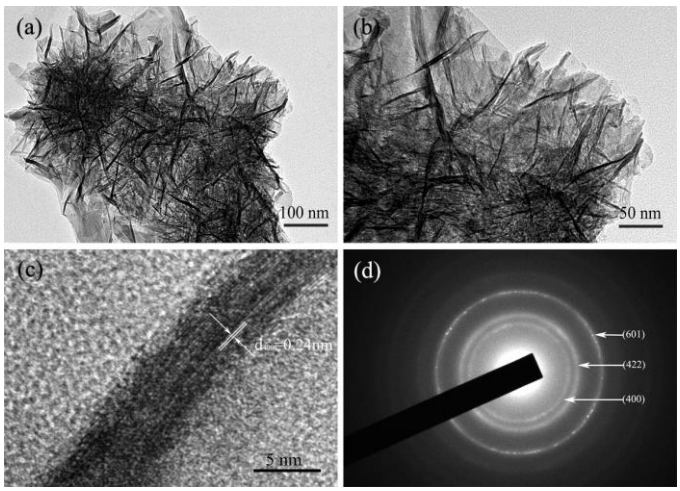

Fig. 3 (a, b) Typical TEM images the $NiMoO_4$@3DGF composites. (c) HRTEM image of the network-strucutred $NiMoO_4$ nanosheets in $NiMoO_4$@3DGF composites. (d) SAED pattern of the $NiMoO_4$ nanosheets scratched from the 3DGF.

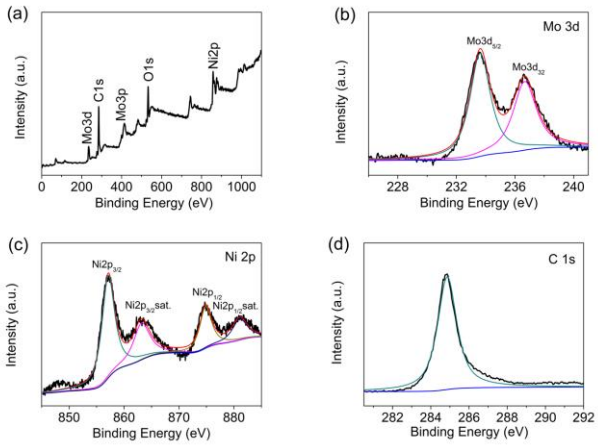

Fig. 4 XPS spectra of (a) survey spectrum, (b) Mo 3d, (c) Ni 2p, and (d) C 1s for $NiMoO_4$@3DGF composites.

mesopores probably results from the release of water molecules during the thermal treatment.[21] The high-resolution TEM (HRTEM) images shown in Fig. 3c reveal a clearly resolved lattice fringes with interplanar spacings of 0.24 nm, corresponding to the (400) plane of $NiMoO_4$. The corresponding selected area electron diffraction (SAED) pattern (as shown in Fig. 3d) indicates the polycrystalline nature of the thin nanosheets, which is consistent with the XRD results.

The chemical composition and the oxidation state of the as-prepared $NiMoO_4$@3DGF composites are identified from XPS measurements and the typical survey spectra are given in Fig. 4. As shown in Fig. 4a, the observed peaks correspond to Ni 2p, Mo 3d, C 1s, and O 1s confirm the presence of Ni, Mo, C and O elements within the as-prepared $NiMoO_4$@3DGF composites, and the absence of other impurities. The Mo 3d and Ni 2p XPS spectra were fitted by using a Gaussian fitting method (Fig. 4b and c). The binding energies of Mo $3d_{3/2}$ and Mo $3d_{5/2}$ peaks are located at 233.5 eV and 236.6 eV can be observed in the region of Mo 3d, respectively. The binding energy and the splitting width ($\triangle$ Mo 3d = 3.1 eV) are characteristics of Mo^{6+} oxidation state in $NiMoO_4$@3DGF.[34,35] The Ni 2p core level spectrum (Fig. 4c) is reasonably deconvoluted into four peaks. The binding energy peak at 857.2 eV and its satellite peak at 862.9 eV correspond to Ni $2p_{3/2}$ level, whereas the binding energy peaks at 874.9 eV and its satellite peak at 881.1 eV correspond to the Ni $2p_{1/2}$ level. The main binding energy peaks of Ni $2p_{3/2}$ and Ni $2p_{1/2}$ are separated by 17.7 eV, which is a signature of the Ni^{2+} oxidation state.[36] Fig. S6 (Supporting Information) shows the high-resolution spectrum of the O 1s region; the binding energy (O 1s) is 532 eV which corresponds to lattice oxygen.[37] Fig. 4d represents the C 1s core level spectrum of the $NiMoO_4$@3DGF composites. The binding energy peak at 284.6 eV correspond to sp^2 hybridized carbon.[38] The XPS results confirm that the valence of Ni, Mo and O elements are +2, +6 and -2, respectively.

The obtained architecture of the network-like $NiMoO_4$@3DGF composites was directly used as a working electrode of CR-2025 coin cell tested without any insulating binder or conducting additive. Nevertheless, as a control experiment for comparison, traditional slurry-coating electrode with $NiMoO_4$ NSS power were also prepared and evaluated, in which $NiMoO_4$ NSS powder were mixed with the conductive carbon black and polyvinylidene fluoride (PVDF) binder in a weight ratio of approximately 8:1:1, and the slurries were coated on Cu foil. Cyclic voltammetry (CV) was first performed to identify the electrochemical reactions occurred during lithiation/delithiation process of the $NiMoO_4$@3DGF composites. Fig. 5a displays the initial five consecutive CV curves of $NiMoO_4$@3DGF electrode at a scan rate of 0.1 mV s^{-1} in the voltage window of 0.005-3.0 V. It is clear from the CV curves that there is substantial difference between the first and subsequent cycles. In the first cycle, there are two obvious irreversible reduction broad peaks at 0.33 and 1.09 V, which can be assigned to Li intercalation into the lattice followed by $NiMoO_4$ crystal structure destruction and formation of the respective nanosize metal particles (reduction of $NiMoO_4$ to metallic Ni and Mo), as well as the decomposition of organic electrolyte to form a solid-electrolyte interphase (SEI) layer at the electrode/electrolyte interphase.[39,40] The first anodic scan shows two peaks at 1.38 and 1.7 V which correspond to the oxidation of metallic Ni and Mo to Ni^{2+} and Mo^{6+}, respectively.[41,42]

In the second and subsequent cycles, two cathodic peaks located at 0.33 and 1.09 V are shifted to 0.58 and 1.39 V, which are induced by the reversible reductive reaction of MoO_3 and NiO to Mo and Ni metal, respectively. The peak intensity and integral areas of the fifth cycle are close to that of the second one for $NiMoO_4$@3DGF electrode, but which are obviously decreased compared with the first cycle. These results indicate that the electrochemical reversibility of $NiMoO_4$@3DGF electrode is gradually built after the first cycle. Thus, on the basis of above CV analysis and the conversion reaction

mechanism of $NiMoO_4$ previous reported, the electrochemical reactions in the as prepared $NiMoO_4$@3DGF composites can be expressed as follows:[43-45]

$$NiMoO_4 + 8Li^+ + 8e^- \rightarrow Ni + Mo + 4Li_2O \quad (1)$$

$$Ni + Li_2O \rightarrow NiO + 2Li^+ + 2e^- \quad (2)$$

$$Mo + 3Li_2O \rightarrow MoO_3 + 6Li^+ + 6e^- \quad (3)$$

$$Ni + Mo + 4Li_2O \leftrightarrow NiO + MoO_3 + 8Li^+ + 8e^- \quad (4)$$

To evaluate the electrochemical performance of the $NiMoO_4$@3DGF electrode, typical voltage-specific capacity curves were recorded at a current density of 100 mA g^{-1} in the voltage range of 0.005-3.0 V vs. Li^+/Li. The charge-discharge profiles of the $NiMoO_4$@3DGF electrode in the initial three cycles at a current density of 100 mA g^{-1} are shown in Fig. 5b. As shown in Fig. 5b, the $NiMoO_4$@3DGF electrode delivered the initial discharge and charge capacities of 1376.96 and 1167.65 mAh g^{-1}, respectively, with an initial columbic efficiency of 84.80%. The irreversible capacity loss is mainly attributed to the incomplete conversion reaction and irreversible lithium loss due to the formation of a solid-electrolyte-interface (SEI) layer and possibly interfacial Li^+ storage, which is inevitable.[46] The columbic efficiency increases rapidly to 97.1% in the second cycle and then remains above 97% in the subsequent cycles. Such a high initial lithium storage capacity might be attributed to the unique 3D graphene-backboned network-like $NiMoO_4$ architectures. The second and third discharge profiles are almost coincided with each other, showing an excellent cycling performance. Besides, the pure 3DGF exhibit quite low capacity (Fig. S7, Supporting Information), indicating that the graphene foam makes little contribution to the total specific capacity of the composite electrode.

The cyclic properties and the discharge capacity cyclability of the $NiMoO_4$@3DGF and $NiMoO_4$ NSS power pasted electrodes were investigated for comparison, as shown in Fig. 5c and d. Surprisingly, the $NiMoO_4$@3DGF electrode worked pretty stably with a reversible discharge capacity as high as 1028.43 mAh g^{-1} after 120 cycles, delivering nearly 89% capacity retention of the second-cycle discharge capacity, as shown in Fig. 5c. Evidently, these results are in stark contrast to those of $NiMoO_4$ NSS power pasted electrode, which show continuous and progressive capacity fading along with the cycling under the same testing conditions, only retaining a discharge capacity of 668.34 mAh g^{-1} after 120 cycles (Fig. 5d).

Additionally, the as-synthesized $NiMoO_4$@3DGF electrode exhibits excellent rate performance. Fig. 5e compares the rate performance of the $NiMoO_4$@3DGF and $NiMoO_4$ NSS power pasted electrodes. For the $NiMoO_4$@3DGF electrode, even cycled at a high current of 3200 mA g^{-1}, a favorable specific capacity of $\sim$ 600 mAh g^{-1} can be maintained. Remarkably, these values are much higher than those of the $NiMoO_4$ NSS power pasted electrode (290 mAh g^{-1}). Moreover, after deep cycling at the high current density of 3200 mA g^{-1}, the specific capacities of $NiMoO_4$@3DGF electrode is nearly recovered to its initial values when the testing current is returned back to 200 mA g^{-1}, indicating the good reversibility and excellent cyclability. On the contrary, the $NiMoO_4$ NSS power pasted electrode shows a lower capacity and worse rate characteristics.

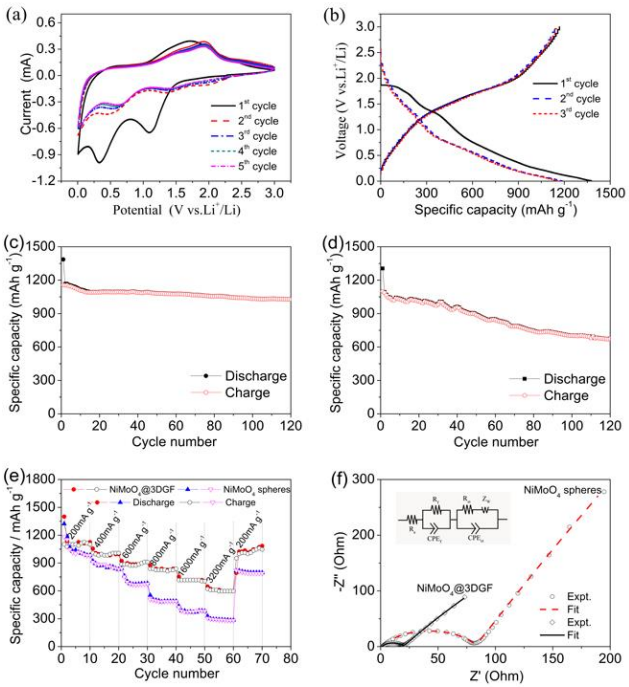

Fig. 5 (a) Cyclic voltammograms of the $NiMoO_4$@3DGF electrode for the initial five cycles at a scan rate of 0.1 mV s^{-1} in the voltage range of 0.005-3.0 V, (b) Galvanostatic charge-discharge voltage profiles of $NiMoO_4$@3DGF electrode for the first three cycles at a current density of 100 mA g^{-1}, (c) Cycling performance of $NiMoO_4$@3DGF electrode at the current density of 200 mA g^{-1}, (d) Cycling performance of $NiMoO_4$ NSS power pasted electrode at the current density of 200 mA g^{-1}, (e) Comparison of rate performance of the $NiMoO_4$@3DGF electrode with $NiMoO_4$ NSS power pasted electrode, (f) Nyquist plots of the $NiMoO_4$@3DGF and $NiMoO_4$ NSS power pasted electrodes measured with an amplitude of 5 mV over the frequency range of 100 kHz and 0.01 Hz (insert corresponding the equivalent circuit model of the studied system).

To gain insight into the reason that the unique 3D graphene-backboned network-like $NiMoO_4$ architectures possesses such excellent electrochemical performances for lithium storage, we performed electrochemical impedance spectroscopy (EIS) for the two electrodes as shown in Fig. 5f. Obviously, the diameter of the semicircle for $NiMoO_4$@3DGF electrode in the high medium frequency region is much smaller than that of the $NiMoO_4$ NSS power electrode, which indicates that $NiMoO_4$@3DGF possess the lowest contact and electron-transfer resistances. The kinetic differences of these $NiMoO_4$ electrodes were further investigated using the common R-C equivalent circuit. The high frequency semicircles in Fig. 5f could be attributed to the SEI layer resistance (R_f) and dielectric relaxation capacitance (CPE_f), the medium frequency semicircles to charge-transfer resistance at the interface between the electrode and electrolyte (R_{ct}), double layer

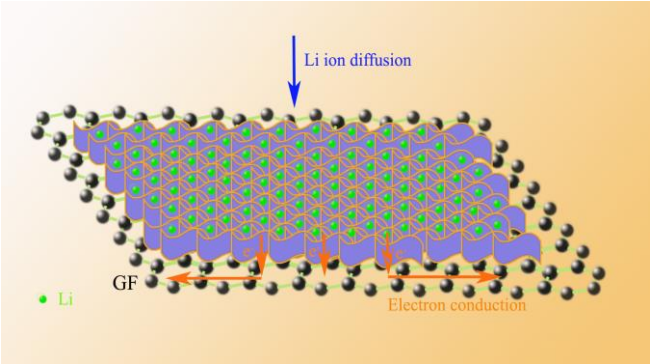

Fig. 6 schematic illustration of network-like $NiMoO_4$@3DGF composites as electrode materials for LIBs.

capacitance (CPE_{ct}), and the inclined line in the low frequency region to lithium-ion diffusion processes. On the basis of the above results, the electrochemical performance of the $NiMoO_4$@3DGF electrode is superior to that of the $NiMoO_4$ NSS power pasted electrode.

The enhanced lithium-ion storage properties and improvement of the high rate performance for $NiMoO_4$@3DGF electrode could be attributed to rationally designed nanostructure and the integrated smart architecture. Specifically, compared with the binder-enriched electrode, directly anchoring interconnected network-like $NiMoO_4$ nanoarchitectures into the skeleton of GF with good mechanical adhesion not only simplifies the electrode processing, but also avoids the use of polymer binder and conducting additives, improving utilization of the electroactive material. In addition, the unique structure also holds the electrode integration and hence mitigates the aggregation and mechanical failure of the active materials after repeated lithiation/delithiation. Moreover, the substrate of highly electrical conductive GF as a current collector can ensure fast electron and ion transportation between the electrolyte and the active material on GF. More importantly, the mesoporous structure and abundant space between the interconnected $NiMoO_4$ nanosheets, which ensures electroactive $NiMoO_4$ nanosheets in high contact with electrolyte and also facilitates fast transportation of lithium ions and electrons into the inner region of the electrode, resulting in an excellent electrochemical performance (As shown in Fig. 6). Benefiting from these advantages, such unique interconnected network-like $NiMoO_4$ nanoarchitectures@3DGF electrode exhibits remarkable electrochemical performance, and hold great promise for high-performance energy storage/conversion applications.

Conclusions

In summary, the as-obtained 3DGF provides a novel substrate for the nucleation and subsequent growth of network-like $NiMoO_4$ nanoarchitectures, in which the porous $NiMoO_4$ nanoarchitectures are well-defined by self assembly of ultrathin nanosheets. The $NiMoO_4$ nanosheets supported on 3D graphene network could be directly evaluated as binder-free, integrated anodes for LIBs. The enhanced lithium-ion storage performance of the electrodes with unique architectures of $NiMoO_4$@3DGF can be attributed to the efficient electron transport channel between the $NiMoO_4$ nanosheets and 3DGF, the shorter Li ion and electron transport pathways, and the enough space to accommodate the volume changes of the $NiMoO_4$ during the cycling. These results indicate that the $NiMoO_4$@3DGF composites are of high promise in developing advanced LIBs with high specific capacity and energy density for practical applications.

Acknowledgements

This work was financially supported by the National Natural Science Foundation of China (Grant No. 51271012) and Innovation Foundation of Beihang University for PhD Graduates. The authors thank the Analysis and Testing Center of the School of Materials Science and Engineering of Beihang University for support.

Notes and references

1 M. Armand, and J. -M. Tarascon, *Nature*, 2008, **451,** 652-657.
2 P. G. Bruce, B. Scrosati, and J -M. Tarascon, *Angew. Chem. Int. Ed.*, 2008, **47,** 2930-2946.
3 B. Dunn, H. Kamath, and J. -M. Tarascon, *Science*, 2011, **334,** 928-935.
4 Y. Chen, M. Zhuo, J. Deng, Z. Xu, Q. Li, and T. Wang, *J. Mater. Chem. A*, 2014, **2,** 4449-4456.
5 N. S. Choi, Z. Chen, S. A. Freunberger, X. Ji, Y. K. Sun, K. Amine, G. Yushin, L. F. Nazar, J. Cho, and P. G. Bruce, *Angew. Chem. Int. Ed.*, 2012, **51,** 9994-10024.
6 X. -L. Huang, R. -Z. Wang, D. Xu, Z. -L. Wang, H.-G Wang, J. -J. Xu, Z. Wu, Q. -C. Liu, Y. Zhang and X. -B. Zhang, *Adv. Funct. Mater.*, 2013, **23,** 4345-4353.
7 Y. M. Sun, X. L. Hu, W. Luo, and Y. H. Huang, *ACS Nano*, 2011, **5,** 7100-7107.
8 X. L. Huang, R. Z. Wang, D. Xu, Z. L. Wang, H. G. Wang, J. J. Xu, Z. Wu, Q. C. Liu, Y. Zhang, and X. B. Zhang, *Adv. Funct. Mater.*, 2013, **23,** 4345-4353.
9 L. Yu, L. Zhang, H. B. Wu, G. Zhang, and X. W. Lou, *Energy Environ. Sci.*, 2013, **6,** 2664-2671.
10 C. Chen, X. Hu, Z. Wang, X. Xiong, P. Hu, Y. Liu, and Y. Huang, *Carbon*, 2014, **69,** 302-310.
11 W. Xiao, J. S. Chen, C. M. Li, R. Xu, and X. W. Lou, *Chem. Mater.*, 2010, **22,** 746-754.
12 T. Tao, A. M. Glushenkov, C. Zhang, H. Zhang, D. Zhou, Z. Guo, H. K. Liu, Q. Chen, H. Hu, and Y. Chen, *J. Mater. Chem*, 2011, **21,** 9350-9355.
13 K. -S. Park, S. -D. Seo, H. -W. Shim, and D. -W. Kim, *Nanoscale Res. Lett.*, 2012, **7,** 35.
14 B. Moreno, E. Chinarro, M. T. Colomer, and J. R. Jurado, *J. Phys. Chem. C*, 2010, **114,** 4251-4257.

15 Y. Huang, X. -L. Huang, J. -S. Lian, D. Xu, L. -M. Wang and X. -B. Zhang, *J. Mater. Chem.*, 2012, **22,** 2844-2847.
16 J. Haetge, I. Djerdj, and T. Brezesinski, *Chem. Commun.*, 2012, **48,** 6726-6728.
17 L. Q. Mai, F. Yang, Y. L. Zhao, X. Xu, L. Xu, and Y. Z. Luo, *Nat. Commun.*, 2011, **2,** 381-385.
18 J. Wang, J. Liu, D. Chao, J. Yan, J. Lin, and Z. X. Shen, *Adv. Mater.*, 2014, **26,** 7162-7169.
19 B. H. Min, D. W. Kim, K. H. Kim, H. O. Choi, S. W. Jang, and H. -T. Jung, *Carbon*, 2014, **80,** 446-452.
20 Z. -L. Wang, D. Xu, H. -G. Wang, Z. Wu, and X. -B. Zhang, *ACS Nano*, 2013, **7,** 2422-2430.
21 X. Yu, B. Lu, and Z. Xu, *Adv. Mater.*, 2014, **26,** 1044-1051.
22 X. Cao, Z. Yin, and H. Zhang, *Energy Environ. Sci.*, 2014, **7,** 1850-1865.
23 Y. M. He, W. J. Chen, X. D. Li, Z. X. Zhang, J. C. Fu, C. H. Zhao, and E. Xie, *ACS Nano*, 2013, **7,** 174-182.
24 X. C. Dong, H. Xu, X. W. Wang, Y. X. Huang, M. B. Chan-Park, H. Zhang, L. H. Wang, W. Huang, and P. Chen, *ACS Nano*, 2012, **6,** 3206-3213.
25 F. Yavari, Z. Chen, A. V. Thomas, W. Ren, H. Cheng, and N. Koratkar, *Sci. Rep.*, 2011, **1,** 166.
26 M. T. Pettes, H. Ji, R. S. Ruoff, and L. Shi, *Nano Lett.*, 2012, **12,** 2959-2964.
27 C. Wang, J. Xu, M. -F. Yuen, J. Zhang, Y. Li, X. Chen, and W. Zhang, *Adv. Funct. Mater.*, 2014, **24,** 6372-6380.
28 S. E. Moosavifard, J. Shamsi, S. Fani, and S. Kadkhodazade, *RSC Adv.*, 2014, **4,** 52555-52561.
29 D. Cai, B. Liu, D. Wang, Y. Liu, L. Wang, H. Li, Y. Wang, C. Wang, Q. Li, and T. Wang, *Electrochim. Acta*, 2014, **115,** 358-363.
30 D. Cai, D. Wang, B. Liu, L. Wang, Y. Liu, H. Li, Y. Wang, Q. Li, and T. Wang, *ACS Appl. Mater. Interfaces*, 2014, **6,** 5050-5055.
31 X. Li, D. Li, Z. Wei, X. Shang, and D. He, *Electrochim. Acta*, 2014, **121,** 415-420.
32 H. Chen, L. Hu, Y. Yan, R. Che, M. Chen, and L. Wu, Adv. Energy Mater., 2013, **3,** 1636-1646.
33 H. Wang, D. Ma, X. Huang, Y. Huang, and X. Zhang, *Sci. Rep*, 2012, **2,** 701.
34 D. Ghosh, S. Giri, and C. K. Das, *Nanoscale*, 2013, **5,** 10428-10437.
35 Z. Xu, Z. Li, X. Tan, C. M. B. Holt, L. Zhang, B. S. Amirkhizab, and D. Mitlin, *RSC Adv.*, 2012, **2,** 2753-2755.
36 W. Hong, J. Wang, P. Gong, J. Sun, L. Niu, Z. Yang, Z. Wang, and S. Yang, *J. Power Sources*, 2014, **270,** 516-525.
37 X. Y. Wu, J. Du, H. B. Li, M. F. Zhang, B. J. Xi, H. Fan, Y. C. Zhu, and Y. T. Qian, *J. Solid State Chem.*, 2007, **180,** 3288-3295.
38 W. B. Yue, S. H. Jiang, W. J. Huang, Z. Q. Gao, J. Li, Y. Ren, X. H. Zhao, and X. J. Yang, *J. Mater. Chem. A*, 2013, **1,** 6928-6933.
39 L. Zhou, D. Zhao, and X. W. Lou, *Adv. Mater.*, 2012, **24,** 745-748.
40 B. Wang, S. Li, J. Liu, M. Yu, B. Li and X. Wu, *Electrochim Acta*, 2014, **146**, 679-687.
41 P. Meduri, E. Clark, J. H. Kim, E. Dayalan, G. U. Sumanasekera, and M. K. Sunkara, *Nano Lett.*, 2012, **12,** 1784-1788.
42 N. N. Leyzerovich, K. G. Bramnik, T. Buhrmester, H. Ehrenberg, and H. Fuess, *J. Power Sources*, 2004, **127,** 76-84
43 C. T. Cherian, M. V. Reddy, S. C. Haur, and B. V. R. Chowdari, *ACS Appl. Mater. Interfaces*, 2013, **5,** 918-923.
44 H. Yu, C. Guan, X. Rui, B. Ouyang, B. Yadian, Y. Huang, H. Zhang, H. E. Hoster, H. J. Fan, and Q. Yan, *Nanoscale*, 2014, **6,** 10556-10561.
45 S. Kim, S. Ogura, H. Ikuta, Y. Uchimoto, and M. Wakihara, Solid State Ionics, 2002, **146,** 249-256.
46 S. -L. Chou, J. -Z. Wang, D. Wexler, K. Konstantinov, C. Zhong, H. -K. Liu, and S. -X. Dou, *J. Mater. Chem*, 2010, **20,** 2092-2098.

Graphical Abstract